A new highly sensitive cryogenic luminescent MOF thermometer built with pyromellitic acid

Thibault Amiaud, Véronique Jubera, Hélène Serier-Brault

ARTICLE

A new highly sensitive cryogenic luminescent MOF thermometer built with pyromellitic acid

Received 00th January 20xx,
Accepted 00th January 20xx

DOI: 10.1039/x0xx00000x

Thibault Amiaud,[a] Véronique Jubera [b] and Hélène Serier-Brault [*a]

A ratiometric thermometer based on a mixed Eu-Tb metal–organic framework is reported with a maximum relative thermal sensitivity of 16.1 % K^{-1} at 11K making this material one of the best-performing thermometers currently reported in the literature. The sensing mechanism of $\{[Tb_{2-x}Eu_x(H_2Btec)(Btec)(H_2O)_2]\cdot 4H_2O\}_n$ (Btec = 1,2,4,5 Benzenetetracarboxylic acid) has been attributed to a phonon-assisted energy migration between neighboring Tb^{3+} ions in the structure.

Introduction

The applications of cryogenic luminescent thermometers span across various fields. In cryogenic research, they play a vital role in studying low-temperature phenomena, such as superconductivity, quantum computing, and fundamental physics research.[1] These thermometers are also extensively employed in the aerospace industry for monitoring and controlling the temperature of cryogenic propellants, coolants, and cryocoolers.[2] Furthermore, they find utility in medical applications, such as monitoring the temperature during cryosurgical procedures and cryopreservation.[3,4]

In recent years, the field of luminescent thermometry has gained significant attention due to its promising applications in various domains, including temperature sensing, biomedicine, environmental monitoring, and energy systems.[5–9] Luminescent thermometers utilize materials that exhibit changes in their luminescent properties in response to temperature variations, enabling precise and non-invasive temperature measurements.

One of the major advantages of luminescent thermometers is their ability to provide remote temperature measurements without the need for physical contact between the probe and the detection device. This feature makes them particularly attractive for applications where direct temperature sensing is challenging or impractical.[10,11]

Among the diverse range of materials explored for luminescence thermometry, Metal-Organic Frameworks (MOFs) have emerged as a highly promising class of materials with exceptional properties for temperature sensing applications.[12]

MOFs are a unique class of hybrid materials composed of metal ions or clusters coordinated by organic ligands, forming porous and crystalline structures with exceptional tunability.[13–15] Lanthanide-based MOFs (LnMOFs) is a sub-class of MOFs with luminescent properties interesting for thermometry.[12,16–18] From the diverse aspects to Ln^{3+}-based luminescence thermometry, one of the most robust methodologies relies on the measurement of the intensity of two transitions of distinct Ln^{3+} emitting centers. In mixed-metal Ln-MOFs, temperature is most often determined from the ratio between the intensity of the $^5D_4 \rightarrow {}^7F_5$ and of the $^5D_0 \rightarrow {}^7F_2$ transitions of the Tb^{3+} and Eu^{3+} ions, respectively.[12,19,20] Mixed Eu-Tb MOFs thermometers are sensitive from the cryogenic domain to the physiological region[21–24], but the number of such materials acting as cryogenic thermometers is very limited (Table 1) and deserves extension, especially to allow a thorough investigation of the structural parameters governing the thermometric properties in these systems.

Herein, we report the synthesis of a new MOF built up from pyromellitic acid (H_4Btec) with a chemical composition $\{[Ln_2(H_2Btec)(Btec)(H_2O)_2]\cdot 4H_2O\}_n$. The thermal behaviour was investigated by multiple techniques (TGA, IR spectroscopy, temperature-dependent XRD) and the crystal structure of the dehydrated material has been solved by single-crystal X-ray diffraction. Finally, two mixed Eu-Tb compounds have been studied as luminescent thermometers and they proved to belong to the most thermally sensitive materials in the cryogenic range. In addition, comparison with other mixed Eu-Tb MOF cryogenic thermometers is performed to highlight the structural similarities between materials, which could explain the same operating temperature range and their high thermal sensitivity.

[a] Nantes Université, CNRS, Institut des Matériaux de Nantes Jean Rouxel, IMN, F-44000 Nantes, France.
[b] CNRS, Bordeaux INP, Institut de Chimie de la Matière Condensée de Bordeaux (ICMCB), UMR 5026, University Bordeaux, F-33600 Pessac, France.

Electronic Supplementary Information (ESI) available: See DOI: 10.1039/x0xx00000x

Results and discussion

1. Structural characterization

The three compounds **Tb-MOF**, **Eu-MOF**, and **Gd-MOF** were obtained in moderate yields as single-crystals or powder using hydrothermal conditions. The powder X-ray diffraction (PXRD) (Figure S1, ESI†) and FTIR measurements (Figure S2, ESI†) indicate that all compounds are isostructural to the $\{[Ln_2(H_2Btec)(Btec)(H_2O)_2]\cdot 4H_2O\}_n$ materials (Ln = Eu, Tb, Gd, Er, Sm) reported in the literature.[25–30] The compound $\{[Ln_2(H_2Btec)(Btec)(H_2O)_2]\cdot 4H_2O\}_n$ crystallises in a monoclinic system with the space group $P2_1/n$ (a = 10.7562(2) Å, b = 7.2075(2) Å, c = 17.2180(5) Å, β = 97.072(2)°). The structure is composed of two Ln^{3+} ions with the same crystallographic site, one H_2Btec^{2-} ligand, one $Btec^{4-}$ ligand, two coordinating water molecules and four non-coordinating water molecules within the cavities of the material. The Ln^{3+} metal centre is nine-coordinated, forming a polyhedron [LnO_9] corresponding to a distorted trigonal tricapped prism. In the structure, each [LnO_9] polyhedron is connected to two other [LnO_9] polyhedra, which are connected by edge-sharing along the b-axis to form a 1D polymeric chain with a shortest Ln-Ln distance of 3.92 Å (Figure 1a). These chains are linked together in the (bc) plane along the c-axis by the $Btec^{4-}$ ligands with a shorter inter-chain distance of 8.84 Å, thus forming a 2D chain plane (Figure 1b). These chains are linked together in the (ac) plane by H_2Btec^{2-} ligands with a shorter Ln-Ln distance of 9.90 Å, forming the final three-dimensional network (Figure 1c). Furthermore, a complex network of hydrogen bonds is present in the pores of the material, between the uncoordinated water molecules, the coordinated water molecules and the non-deprotonated carboxyl groups.

The mixed compounds denoted by $\mathbf{Tb_{2-x}Eu_x}$ (x = 0.02, 0.06, 0.10, 0.20) were obtained in moderate yields as a white microcrystalline powder. The obtained molar ratio was determined by ICP-AES, (Table S1, ESI†). Both PXRD analyses (Figure S3, ESI†)) and FT-IR spectroscopy (Figure S4, ESI†)) confirm that the mixed compounds are isostructural with the monometallic compounds.

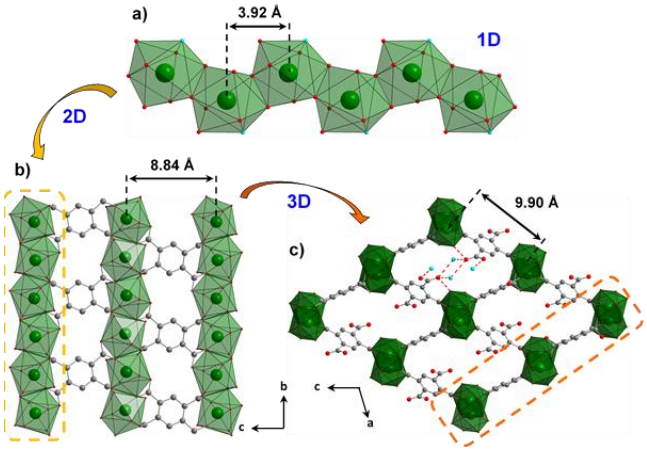

Figure 1. a) Fragment of the 1D polymer chain of the **Tb-MOF** compound showing the edge-sharing connections between the [TbO_9] polyhedra. b) Projection of the chains along the c-axis connected by $Btec^{4-}$ ligands in the (bc) plane and c) Connection of the chains by H_2Btec^{2-} ligands along the a-axis in the (ac) plane. Colour code: green = [TbO_9] polyhedron, red = oxygen of the ligand, cyan = oxygen of the coordinated and non-coordinated water molecules and grey = carbon. The hydrogen-bonding network is partially shown in red dotted lines. Hydrogen atoms are omitted for clarity.

2. Thermal behaviour

The thermal behavior of as-synthesized solids was first analyzed by thermogravimetric analyses (Figure S5, ESI†). The thermal decomposition of all compounds proceeds through a multistep process, which is completed at a quite low temperature (~ 550°C). The first step that is related to the removal of the 4 non-coordinated water molecules in hydrogen interaction with the carboxylate functions of the ligand appears from 30 to 120 °C and corresponds to about 7.8% of the material total mass. This value is in good agreement with the calculated value for compound $\{[Ln_2(H_2Btec)(Btec)(H_2O)_2]\cdot 4H_2O\}_n$. The second step, from 160 to 240°C, is associated with the removal of the two coordinated water molecules that are more strongly bound to the Ln^{3+} ions (theoretical value: 3.9%, experimental value : 4.1%). Finally, the last step that is completed at ~ 550°C is attributed to the decomposition of the ligand leading to the formation of the Ln_2O_3 oxide (calculated residue = 38.3% (for Eu), experimental: 38.5%). Furthermore, the compound **Gd-MOF** seems to have a better thermal stability as the mass loss corresponding to the degradation of the ligand occurs between 460 and 630 °C, i.e. about 100 °C higher than for the compound **Eu-MOF**. This may be due to a higher dissociation energy (E_{diss}) of the Ln-O bond when Ln = Gd^{3+}, as reported in the literature (E_{diss}(Gd-O) > E_{diss}(Tb-O) > E_{diss}(Eu-O)).[31–33]

Temperature dependent powder X-ray diffraction was carried on **Tb-MOF** between 30 and 300°C under air (Figure S6, ESI†). Thus, the structure remains intact up to 50 °C to dehydrate gradually from 60°C to 90°C. Then, from 90°C the dehydrated phase $\{[Tb_2(H_2Btec)(Btec)(H_2O)_2]\}$ (**Tb-MOF-dhy**) is obtained as single phase, which is stable until 140°C. The second dehydration process occurs from 150°C and is totally completed at 160°C to provide a non-hydrated phase, $\{[Tb_2(H_2Btec)(Btec)]\}$, stable up to 300°C.

To obtain the crystal structure of the dehydrated phase (**Tb-MOF-dhy**), single-crystal diffraction was used on a crystal of **Tb-MOF**, which was gently heated until 90°C. The crystal remains intacts, and the crystal structure was resolved. Thus, the compound **Tb-MOF-dhy** crystallises in a monoclinic system with the space group $P2_1/n$ (a = 16.8704(7) Å, b = 7.2155(2) Å, c = 18.3095(5) Å, β = 104.552(4)°) (Table S2). The material is composed of two crystallographically independent Tb^{3+} cations, one H_2Btec^{2-} ligand, one $Btec^{4-}$ ligand and two coordinating water molecules.

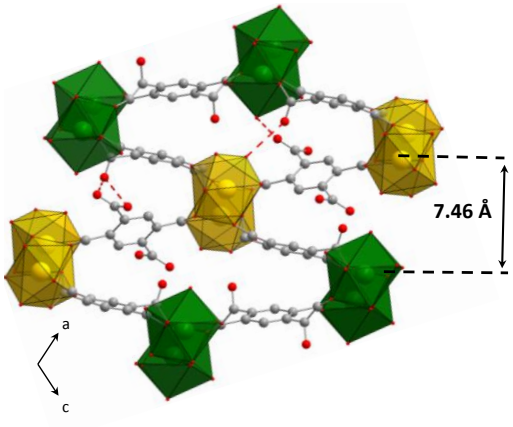

Figure 2. Representation in the (ac) plane of the crystal structure of **Tb-MOF-dhy**, $[Tb(1)O_9]$ and $[Tb(2)O_9]$ chains are running along the b-axis. Colour code: yellow = $[Tb(1)O_9]$ polyhedron, green = $[Tb(2)O_9]$ polyhedron, red = oxygen and grey = carbon. The hydrogen-bonding network is partially shown in red dotted lines. Hydrogen atoms are omitted for clarity.

Both Tb^{3+} centre are nine-coordinated, forming in one case a distorted trigonal tricapped prism (Tb(1)) with oxygen atoms from four ligands and one water molecule, and in another case forming a trigonal tricapped prism (Tb(2)) whose oxygen atoms originate from six organic ligands and one water molecule. In the structure, each $[Tb(1)O_9]$ polyhedron is connected to two other $[Tb(1)O_9]$ polyhedra by edge-sharing along the b-axis to form a 1D polymeric chain with a shortest distance Tb(1)-Tb(1) of 3.9363(13) Å. Similarly, $[Tb(2)O_9]$ polyhedra form another 1D polymeric chain with a shorter distance Tb(2)-Tb(2) of 3.9503(13) Å. The chains of $[Tb(1)O_9]$ and $[Tb(2)O_9]$ polyhedra are connected to each other by the ligands in the (bc) plane along the c-axis, to finally form a 3D network, with the shortest Tb(1)-Tb(2) distance of 7.4620(15) Å (Figure 2). Clearly, the removal of water molecules located in the cavities leads to a contraction and a slight distortion of the **Tb-MOF** structure, preventing the presence of any permanent porosity. Finally, after dehydration, the reverse process of rehydration is almost spontaneous as the initial Tb-MOF starts to be recovered after 16h of exposition under air to be totally recovered after an exposition of 60h (Figure S7, ESI†). Thus, the low stability of the dehydrated phase prevents the study of luminescence properties according to the temperature, and the comparison with the pristine material.

3. Room-temperature luminescence properties

First, the phosphorescence spectrum (Figure S8, ESI†) of **Gd-MOF** was recorded to identify the lowest-lying triplet energy state positioning of the organic ligand. Then, the triplet level is estimated to be 24272 cm^{-1} from the shortest-wavelength, which is in a suitable energy range to sensitize both Eu^{3+} and Tb^{3+} according to the Latva's empirical rule.[34] Photoluminescence properties of **Tb-MOF**, **Eu-MOF**, and their mixed Eu-Tb compounds have been characterized in the solid-state at room temperature. Upon UV excitation at 309 nm, the emission spectrum of **Tb-MOF** displays the typical f-f lines at 490, 545, 581, and 619 nm attributed to the $^5D_4 \rightarrow {}^7F_{6\text{-}3}$ transitions of Tb^{3+}, while the emission spectrum of **Eu-MOF** is composed by the $^5D_0 \rightarrow {}^7F_{0\text{-}4}$ transitions centred at 587, 611, 652, and 645 nm (Figures S9 and S10, ESI†). Furthermore, the emission bands of the ligand are completely absent in the luminescent spectra of both compounds, evidencing an efficient sensitization of both Tb^{3+} and Eu^{3+} ions by the organic ligand (Figure 3b). The bimetallic compounds **$Tb_{2-x}Eu_x$-MOF** exhibit the f-f transitions lines of both Tb^{3+} and Eu^{3+} ions (Figures 3 and S11, ESI†). The increase of Eu^{3+} content leads to a gradual shift from pure green emission (**Tb-MOF**) to almost pure red emission (**Eu-MOF**) when x = 0.020 (Figure S12 and Table S3, ESI†). This shift in the color coordinates is caused by the Tb^{3+}-to-Eu^{3+} energy transfer, which was evidenced by the presence of the $^7F_6 \rightarrow {}^5D_4$ absorption band (at ~ 480 nm) of Tb^{3+} within the $^5D_0 \rightarrow {}^7F_2$ Eu^{3+} transition in the excitation spectra of mixed compounds (Figures 3a and S11, ESI†).

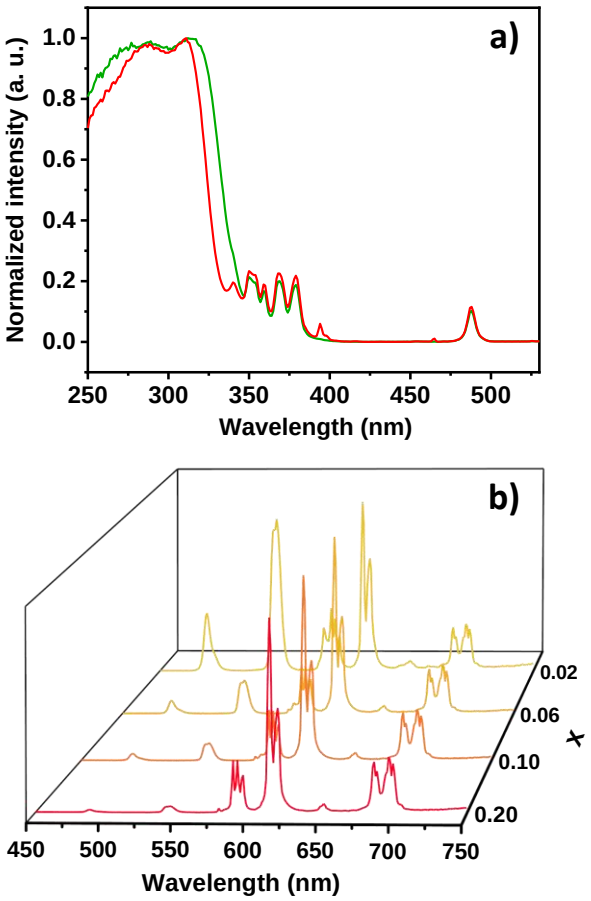

Figure 3. (a) Room temperature excitation spectra of $Tb_{1.98}Eu_{0.02}$-MOF monitoring at 614 nm ($^5D_0 \rightarrow {}^7F_2$ transition of Eu^{3+}, red line) and at 544 nm ($^5D_4 \rightarrow {}^7F_5$ transition of Tb^{3+}, green color), and (b) Room temperature emission spectrum of **$Tb_{2-x}Eu_x$-MOF** monitoring at 309 nm.

In mixed compounds, the Tb^{3+}-to-Eu^{3+} energy transfer efficiencies (η_{ET}) were determined at room temperature from the following equation:[35–38]

$$\eta_{ET} = 1 - \frac{\tau}{\tau_0} \qquad \text{(eq 1)}$$

where τ and τ_0 correspond to the lifetime of the donor (Tb^{3+}) in the presence and absence of the acceptor (Eu^{3+}), respectively (Table S4, ESI†). The $^5D_4$ (monitored at 544 nm) and $^5D_0$ (monitored at 614 nm) decay curves of single-doped and mixed samples were perfectly described by single exponential functions. The lifetime of Tb^{3+} ion rapidly decreases from 525 µs for the compound **$Tb_{1.98}Eu_{0.02}$-MOF** to 194 µs for **$Tb_{1.80}Eu_{0.20}$-MOF** suggesting an important energy transfer between both emitters. Moreover, increasing the europium content leads to a rapid shift from the green color of **Tb-MOF**, with (x; y) coordinates equal to (0.342; 0.575), to the red color of **Eu-MOF** ((x; y) = (0.653; 0.347)). Consequently, as supposed by the rapid evolution of CIE coordinates and the abrupt decrease of $^5D_4$ lifetime with the increase of Eu^{3+} (Figures S12, ESI†), the Tb^{3+}-to-Eu^{3+} energy transfer is relatively high, varying from 63%, for x = 0.02, to 86%, for x = 0.20 (Figures S13, ESI†). The short Ln-Ln distance in the 1D polymeric chain and between two adjacent chains is the cause of this high energy-transfer efficiency.

4. Thermometric properties

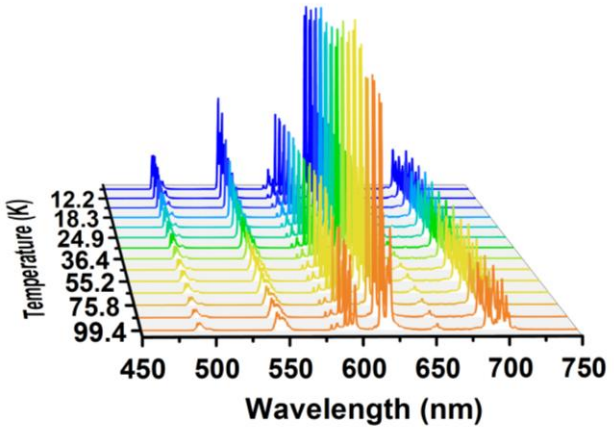

Figure 4. Temperature-dependent emission spectra in the 10-100K range for upon 309 nm excitation of **$Tb_{1.90}Eu_{0.10}$-MOF.**

The thermometric properties were investigated using the emission spectra in the 10-100K for the compounds **$Tb_{2-x}Eu_x$-MOF**, with x = 0.10 and 0.20 (Figures 4 and S14, ESI†). The integrated areas of the $^5D_4 \rightarrow {}^7F_5$ (I_{Tb}) and $^5D_0 \rightarrow {}^7F_2$ (I_{Eu}) emissions were used to define the thermometric parameter as $\Delta = I_{Tb}/I_{Eu}$. The I_{Tb} and I_{Eu} areas were integrated using the emission spectra in the 535–560 nm and 605–635 nm intervals, respectively. The temperature dependence of emission spectra and the thermal dependence of integrated intensities are presented in Figure 5a and Figure S14, ESI† for the materials **$Tb_{1.90}Eu_{0.10}$-MOF**, and **$Tb_{1.80}Eu_{0.20}$-MOF**, respectively. For both samples, the Tb^{3+} emission abruptly decreases from 10 to 50K to reach a plateau until 100K, while the Eu^{3+} emission slightly increases over the whole temperature range. The thermometric parameter $\Delta = I_{Tb}/I_{Eu}$ (Figure 5b and Figure S15**,** ESI†) is depicted according to the temperature and may be described by the phenomenological Mott-Seitz expression involving a unique non-radiative recombination channels (assuming a temperature dependence of the Eu^{3+} emission smaller than that of the Tb^{3+} emission):

$$\Delta = \frac{I_{Tb}}{I_{Eu}} = \frac{\Delta_0}{1+\alpha\, exp\ (-\Delta E_{Tb}/k_B T)} \qquad \text{(eq 2)}$$

where Δ_0 is the Δ parameter at T=0 K, $\alpha = W_0/W_R$ is the ratio between the nonradiative (W_0 at T=0 K) and radiative (W_R) rates, and ΔE_{Tb} is the activation energy for the non-radiative channel. Fitting the experimental Δ values to equation 2, yields Δ_0 = 1.8 ± 0.7, α = 14 ± 5, ΔE_{Tb} = 17 ± 2 cm^{-1} for **$Tb_{1.90}Eu_{0.10}$-MOF**, and Δ_0 = 1.0 ± 0.1, α = 17 ± 2, ΔE_{Tb} = 17 ± 1 cm^{-1} for **$Tb_{1.80}Eu_{0.20}$-MOF**. Thus, similar values were observed for α and ΔE_{Tb} for both samples, assuming that the same non-radiative T-dependent deactivation pathway occurs for both compositions. These low ΔE_{Tb} values are generally assigned to phonon-assisted energy migration between two nearby Tb^{3+} centers, as already reported in the literature for MOFs thermometers highly sensitive in the cryogenic range[39,40], suggesting that this non-radiative deactivation pathway is predominant in Eu-Tb MOFs cryogenic thermometers. Furthermore, Tb^{3+}-Tb^{3+} energy migration seems to be favored when the Ln-Ln distances are very short, which is the case for the **$Tb_{2-x}Eu_x$-MOF** materials (d_{Ln-Ln} = 3.92Å) and in the MOF reported by Liu *et al.*[40], $Tb_{0.95}Eu_{0.05}HL$ (H4L = 5-hydroxy-1,2,4-benzenetricarboxylic acid) where the distance between two adjacent Ln^{3+} cations is 4.212 Å. Thus, mixed Eu-Tb MOFs that are highly sensitive in the cryogenic temperatures present structural similarities, and efforts must be concentrating to confirm these initial assumptions.

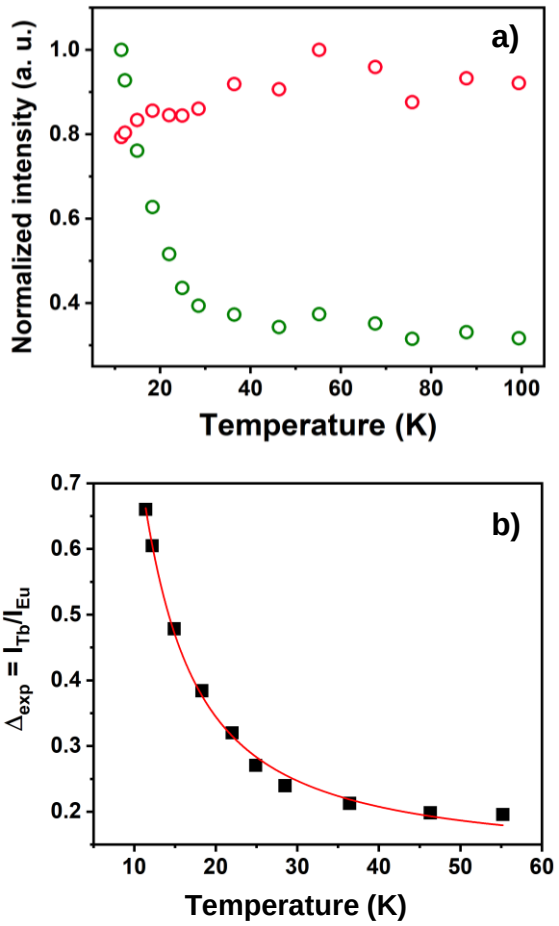

Figure 5. a) Temperature dependence of the normalized integrated area of I_{Tb} (green points) and I_{Eu} (red points) of **$Tb_{1.90}Eu_{0.10}$-MOF** upon 309 nm excitation, and b) Temperature-dependence of the thermometric parameter Δ in the 10-55K range for the compound **$Tb_{1.90}Eu_{0.10}$-MOF** excited at 309 nm. The red line represents the calibration curve obtained by the best fit of the experimental points to the equation 1 (r^2> 0.99).

The corresponding relative thermal sensitivity, defined as $S_r = |\partial\Delta/\partial T|/\Delta$ and used as a figure of merit to compare the performance of distinct systems[9,12,41] is plotted in Figure 6. Thus, as luminescent ratiometric thermometers, both materials exhibits a very good thermal sensitivity in the cryogenic range (100 K < T), with a maximum relative sensitivity (S_m) equal to 14.5 and 16.1 $\%K^{-1}$ at 11K for **$Tb_{1.90}Eu_{0.10}$-MOF** and **$Tb_{1.80}Eu_{0.20}$-MOF**, respectively. Consequently, both materials are very competitive with the most sensitive material in the cryogenic range so far, as on can see on Table 1.[40]

Table 1. Maximum relative temperature sensitivity S_m (% K^{-1}) and corresponding T_m (K) of the Eu^{3+}/Tb^{3+} MOFs reported in the cryogenic range.

Materials	S_m (% K^{-1})	T_m	Ref.
$\{[Tb_{1.87}Eu_{0.13}(HY)_2(H_2O)_3]\cdot 5H_2O\}$	31	4	[40]
$\{[Tb_{0.914}Eu_{0.086}(pda)_3(H_2O)]\cdot 2H_2O\}$	5.96	25	[42]
$\{[Tb_{0,898}Eu_{0,102}(notp)(NO_3)(H_2O)]\cdot 8H_2O\}$	3.90	38	[43]
$\{[Tb_{0,9}Eu_{0,1}(bdc)_3(H_2O)_2]\cdot H_2O\}$	3.30	36	[39]
$\{[Tb_{0,95}Eu_{0,05}(btb)(H_2O)]\cdot(H_2O)_x\cdot(CH_3OH)_x\}$	2.85	14	[44]
$\{[Tb_{1.90}Eu_{0.10}(H_2Btec)(Btec)(H_2O)_2]\cdot 4H_2O\}_n$	14.5	11	This work
$\{[Tb_{1.80}Eu_{0..20}(H_2Btec)(Btec)(H_2O)_2]\cdot 4H_2O\}_n$	16.1	11	This work

HY = 5-hydroxy-1,2,4-benzenetricarboxylic acid, pda = 1,4-phenyldiacetic acid, notp = 1,4,7-triazacyclononane-1,4,7-triyl-tris(methylenephosphonic acid) , bdc = 1,3-benzendicarboxylic acid, btb = 1,3,5-tris(4-carboxyphenyl)benzene

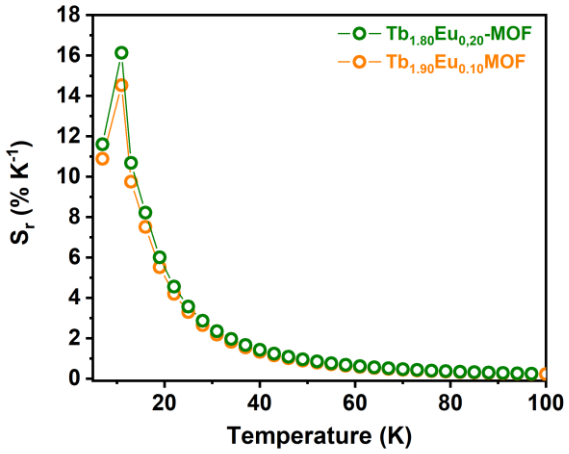

Figure 6. Relative thermal sensitivity in the 10-100K range for the materials **$Tb_{1.90}Eu_{0.10}$-MOF**, and **$Tb_{1.80}Eu_{0.20}$-MOF**.

The temperature uncertainty, $\delta T = 1/S_r \times \delta\Delta/\Delta$, defines the smallest temperature change that may be ascertained in a given measurement, where $\delta\Delta/\Delta$ is the relative error in the determination of the thermometric parameter and depends mostly on the acquisition setup.[45] The δT value was not experimentally determined, and given the used detector, we chose for $\delta\Delta/\Delta$, the typical value for a photomultiplier, i.e. $\delta\Delta/\Delta$=0.20%. However, this corresponds to the lower uncertainty limit, but the real experimental values is undoubtedly higher.[45] Consequently, a minimum temperature uncertainty of 0.012 K (0.016K) at 11 K and a maximum of 0.80 K (0.88 K) at 70 K, could be obtained (Figure S16, ESI†) for **$Tb_{1.80}Eu_{0.20}$-MOF (Tb$_{1.90}$Eu$_{0.10}$-MOF)**. Temperature cycling between 10 and 70 K (Figure S17, ESI†) demonstrates repeatability better than 99% at 70K for **$Tb_{1.80}Eu_{0.20}$-MOF**.

Conclusions

We have synthesized a mixed Eu-Tb metal–organic framework, which can be used as a luminescent thermometer in cryogenic temperatures (< 100 K). The thermometric performances relies on phonon-assisted energy migration between two adjacent Tb^{3+} ions. **$Tb_{1.90}Eu_{0.10}$-MOF** and **$Tb_{1.80}Eu_{0.20}$-MOF** exhibit a very good thermal sensitivity in the range 10–50 K with a relative sensitivity up to 36% K^{-1} at 11 K, leading to one of the best-performing thermometers currently reported in the literature.

Noticeably, the same deactivation pathway governs the thermometric properties of the two most sensitive mixed Eu-Tb MOFs in the cryogenic domain, i.e energy migration, which seems being favoured by short Ln-Ln bond distances.

Author Contributions

T. Amiaud performed the syntheses of compounds and their main characterizations (PXRD, TGA, FTIR, room-temperature luminescence analyses). V. Jubera carried out the temperature-dependence luminescence measurements. H. Serier-Brault managed the project and prepared the draft manuscript. All authors participated in the writing, reviewing and editing the final version of the manuscript.

Conflicts of interest

There are no conflicts to declare

Acknowledgements

The French National Research Agency (ANR), as part of the THERMOF project (ANR- 18-CE09-0008-01), supported this work.

Notes and references

1 R. L. Rusby and M. Kempson, *Rev. Générale Therm.*, 1996, **35**, 338–343.

2 K. Kinefuchi, T. Miyakita, Y. Umemura, J. Nakajima and M. Koga, *Cryogenics (Guildf).*, 2022, **124**, 103494.

3 Y. Rabin and A. Shitzer, *Cryobiology*, 1996, **33**, 82–92.

4 J. C. Gilbert, B. Rubinsky, S. T. S. Wong, K. M. Brennan, G. R. Pease and P. P. Leung, *Magn. Reson. Imaging*, 1997, **15**, 657–667.

5 M. Quintanilla, L. M. Liz-Marzán and L. M. Liz-Marzan, *Nano Today*, 2018, **19**, 126–145.

6 C. D. S. Brites, S. Balabhadra and L. D. Carlos, *Adv. Opt. Mater.*, 2019, **7**, 1–30.

7 L. D. Carlos and F. Palacio, *Thermometry at the nanoscale, Techniques and Selected applications*, Royal Society of Chemistry, Oxforshire, 2016.

8 C. D. S. Brites, P. P. Lima, N. J. O. Silva, A. Millan, V. S. Amaral, F. Palacio and L. D. Carlos, *Nanoscale*, 2012, **4**, 4799–4829.

9 M. D. Dramicanin, *J. Appl. Phys.*, 2020, **128**, 40902.

10 B. del Rosal, D. Ruiz, I. Chaves-Coira, B. H. Juárez, L. Monge, G. Hong, N. Fernández and D. Jaque, *Adv. Funct. Mater.*, 2018, **28**, 1806088.

11 S. Lal, J. Verma and C. J. F. Van Noorden, *Int. J. Nanomedicine*, 2014, **9**, 2863.

12 J. Rocha, C. D. S. Brites and L. D. Carlos, *Chem. - A Eur. J.*, 2016, **22**, 14782–14795.

13 H. Li, M. Eddaoudi, M. O'Keeffe and O. M. Yaghi, *Nature*, 1999, **402**, 276–279.

14 P. Horcajada, R. Gref, T. Baati, P. K. Allan, G. Maurin, P. Couvreur, G. Férey, R. E. Morris and C. Serre, *Chem. Rev.*, 2012, **112**, 1232–1268.

15 N. L. Rosi, J. Kim, M. Eddaoudi, B. Chen, M. O'Keeffe and O. M. Yaghi, *J. Am. Chem. Soc.*, 2005, **127**, 1504–1518.

16 A. Cadiau, C. D. S. Brites, P. M. F. J. Costa, R. A. S. Ferreira, J. Rocha and L. D. Carlos, *ACS Nano*, 2013, **7**, 7213–7218.

17 I. N'Dala-Louika, D. Ananias, C. Latouche, R. Dessapt, L. D. Carlos and H. Serier-Brault, *J. Mater. Chem. C*, 2017, **5**, 10933–10937.

18 V. Trannoy, A. N. Carneiro Neto, C. D. S. Brites, L. D. Carlos and H. Serier-Brault, *Adv. Opt. Mater.*, 2021, **9**, 1–12.

19 Y. Cui, H. Xu, Y. Yue, Z. Guo, J. Yu, Z. Chen, J. Gao, Y. Yang, G. Qian and B. Chen, *J. Am. Chem. Soc.*, 2012, **134**, 3979–3982.

20 X. Rao, T. Song, J. Gao, Y. Cui, Y. Yang, C. Wu, B. Chen and G. Qian, *J. Am. Chem. Soc.*, 2013, **135**, 15559–15564.

21 T. Xia, Z. Shao, X. Yan, M. Liu, L. Yu, Y. Wan, D. Chang, J. Zhang and D. Zhao, *Chem. Commun.*, , DOI:10.1039/D1CC00297J.

22 F. Vanden Bussche, A. M. Kaczmarek, J. Schmidt, C. V Stevens and P. Van Der Voort, *J. Mater. Chem. C*, , DOI:10.1039/C9TC02328C.

23 D. Mara, F. Artizzu, B. Laforce, L. Vincze, K. Van Hecke, R. Van Deun and A. M. Kaczmarek, *J. Lumin.*, 2019, **213**, 343–355.

24 T. Chuasaard, A. Ngamjarurojana, S. Surinwong, T. Konno, S. Bureekaew and A. Rujiwatra, *Inorg. Chem.*, 2018, **57**, 2620–2630.

25 C. De Wu, C. Z. Lu, W. Bin Yang, S. F. Lu, H. H. Zhuang and J. S. Huang, *Eur. J. Inorg. Chem.*, 2002, **2**, 797–800.

26 R. Cao, D. Sun, Y. Liang, M. Hong, K. Tatsumi and Q. Shi, *Inorg. Chem.*, 2002, **41**, 2087–2094.

27 M. L. Hu, N. W. Zhu, X. H. Li and F. Chen, *Cryst. Res. Technol.*, 2004, **39**, 505–510.

28 M. Tabatabaee, R. Mohammadinasab and M. Aghaie, *J. Inorg. Organomet. Polym. Mater.*, 2016, **26**, 127–133.

29 Q. B. Bo, Z. X. Sun, Y. L. Sheng, Z. W. Zhang, G. X. Sun, C. L. Chen, Y. X. Li and D. Q. Wang, *Struct. Chem.*, 2006, **17**, 609–615.

30 Y. Acar, *Anadolu Univ. J. Sci. Technol. A - Appl. Sci. Eng.*, 2016, **17**, 754–765.

31 Cottrell T. L., *J. Am. Chem. Soc.*, 2002, **77**, 2350–2350.

32 J. K. Gibson, *J. Phys. Chem. A*, 2003, **107**, 7891–7899.

33 L. L. Ames, *J. Phys. Chem.*, 1967, **71**, 2707–2718.

34 M. Latvaa, H. Takalob, V. M. Mukkala, C. Matachescuc, J. C. Rodriguez-ubisd, J. Kankarea, M. Latva, H. Takalob, V. M. Mukkala, C. Matachescu, J. C. Rodríguez-Ubis and J. Kankare, *J. Lumin.*, 1997, **75**, 149–169.

35 L. J. Charbonniere, N. Hildebrandt, R. F. Ziessel and H.-G. Loehmannsroeben, *J. Am. Chem. Soc.*, 2006, **128**, 12800–12809.

36 A. N. Carneiro Neto, R. T. Moura, A. Shyichuk, V. Paterlini, F. Piccinelli, M. Bettinelli and O. L. Malta, *J. Phys. Chem. C*, 2020, **10**, 10105–10116.

37 H.-Y. D. Ke and E. R. Birnbaum, *J. Lumin.*, 1995, **63**, 9–17.

38 R. Reisfeld, Springer, Berlin, Heidelberg, 1973, pp. 53–98.
39 I. N'Dala-Louika, D. Ananias, C. Latouche, R. Dessapt, L. D. Carlos and H. Serier-Brault, *J. Mater. Chem. C*, 2017, **5**, 10933–10937.
40 X. Liu, S. Akerboom, M. De Jong, I. Mutikainen, S. Tanase, A. Meijerink and E. Bouwman, *Inorg. Chem.*, 2015, **54**, 11323–11329.
41 C. D. S. Brites, P. P. Lima, N. J. O. Silva, A. Millán, V. S. Amaral, F. Palacio and L. D. Carlos, *New J. Chem.*, 2011, **35**, 1177.
42 Z. Wang, D. Ananias, A. Carné-Sánchez, C. D. S. Brites, I. Imaz, D. Maspoch, J. Rocha and L. D. Carlos, *Adv. Funct. Mater.*, 2015, **25**, 2824–2830.
43 M. Ren, C. D. S. Brites, S. Bao, R. A. S. Ferreira and L. Zheng, 2015, **898**, 8480–8484.
44 D. Ananias, C. D. S. Brites, L. D. Carlos and J. Rocha, *Eur. J. Inorg. Chem.*, 2016, **2016**, 1967–1971.
45 C. D. S. Brites, A. Millán and L. D. Carlos, in *Handbook on the Physics and Chemistry of Rare Earths*, 2016, vol. 49, pp. 339–427.